

Research Article

Finite-Element Simulation on NPGCS Precast Shear Wall Spatial Structure Model

Dongyue Wu ¹, Shuting Liang ², Mengying Shen,³ Zhengxing Guo,³ Xiaojun Zhu,⁴ Chongfang Sun,⁵ and Qian Fu⁶

¹School of Civil Engineering and Architecture, Jiangsu University of Science and Technology, Zhenjiang, Jiangsu, China

²Zhenjiang Archives, Zhenjiang, Jiangsu, China

³School of Civil Engineering, Southeast University, Nanjing, Jiangsu, China

⁴Architects and Engineers Co., Ltd., Southeast University, Nanjing, Jiangsu, China

⁵Jinan Rail Transit Group Co., Ltd., Jinan, Shandong, China

⁶School of Information Engineering, Nanjing Audit University, Nanjing, Jiangsu, China

Correspondence should be addressed to Dongyue Wu; dywu@just.edu.cn

Received 5 July 2018; Accepted 22 October 2018; Published 13 March 2019

Academic Editor: Yinshan Tang

Copyright © 2019 Dongyue Wu et al. This is an open access article distributed under the Creative Commons Attribution License, which permits unrestricted use, distribution, and reproduction in any medium, provided the original work is properly cited.

Seismic performance is basically required in precast shear wall. This study focuses on evaluation and improvement on precast shear wall seismic performance. By carrying out the finite-element simulation on a precast shear wall spatial model with new connector from a practical high-rise precast residential building, which was named as NPGCS and experimentally tested by low-cyclic reversed lateral loads in early studies, the performance results including strengths, stiffness, stress, and concrete damage ratio distributions were obtained, and the reliability of NPGCS spatial model was verified. According to the testing results, the finite-element simulation for the NPGCS spatial model is reliable and relatively accurate, especially for applying contact and beam elements into numerical analysis of precast interfaces and dowel shear actions, respectively. The strengths, stiffness, stress, and concrete damage ratio distributions from the simulation also supported the experimental results and conclusions.

1. Introduction

Precast technologies have advances in industrial production, environmental protection, and high mechanical reliability, and so on, but the following two reasons put serious limitations on precast technology application in China: (1) as most territory of China is in seismic area, there are stricter seismic design requirements and (2) due to the high population of dentist in south eastern China, most of the Chinese residential building is high-rise shear wall structure with 20–33 floors, which will enlarge the seismic loads dramatically [1]. Even some new grouted precast connectors provide very good connector performance, special manufacture is required, which dramatically increased application costs [2–6].

To reduce manufacture cost while achieving good connecting properties, a new connector of NPGCS (new

pore-forming grouted connector with welded closure confinement steels) was invented in early research [7], which only uses the widely applied normal steel bars and the preburied thin metal pore to replace or partially replace the expensive grouted steel sleeve and to reduce the manufacture cost [8, 9]. The NPGCS is composed of the buckle-configured confinement steel bars, connecting overlapped steel bars, thin metal pore, and grouting materials. Figure 1 is the steel bar configuration of NPGCS. The manufacture process has no special required part and includes steel cage fabrication, concrete casting and curing, precast components assemble, grouting, and curing.

Four basic design criteria required in NPGCS are as follows: (1) the arc butt welding approach should be applied in welded closure steel bar hoops manufacture and the tension strength of welded joint should be no less than that of single continues steel bar with same strength grade and

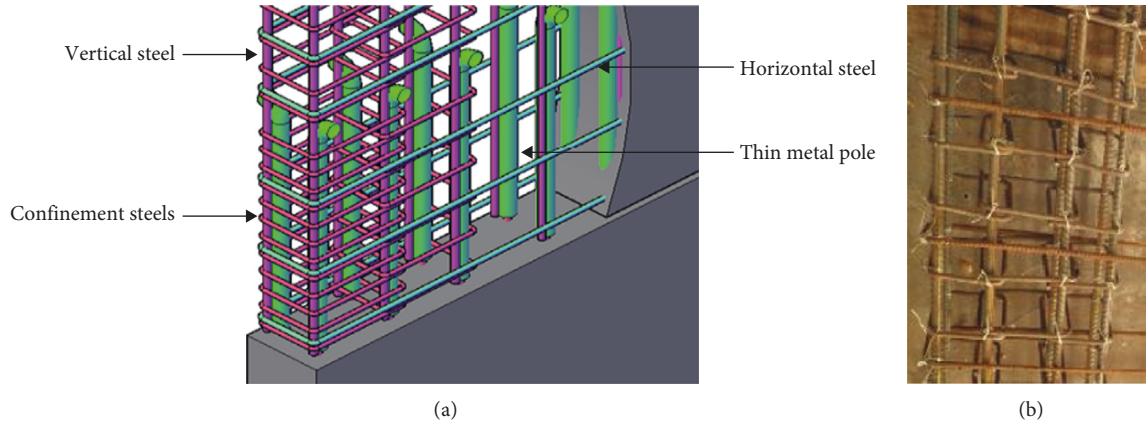


FIGURE 1: The NPGCS steel bars configuration. (a) Steel bars configurations. (b) Steel bars configurations in reality.

diameter. (2) The confinement steel hoops should be arranged in buckle configuration, by which to generate superposed area by adjacent two confinement steel bar hoops in horizontal direction and to provide sufficient confinement stress onto the grouting materials and the overlapped connecting steel bars shown in Figure 2. (3) In vertical direction, the confinement steel hoops in shear wall marginal area will be strengthened by reducing adjacent confinement steel hoops distance into half. (4) The basic length of overlapped connecting steel bars and the strength of concrete and steel bar should be satisfied to the “Code for design of concrete structures” applied in China [10]. It is also required that the grouting material should be early strength with higher than 35 MPa for 1 day, 60 MPa for 3 days, and 85 MPa for 28 days according to the “Technical specification for grout sleeve splicing of rebars” [11] and the “Technical standard for assembled buildings with concrete structure” [12].

Early experimental test on single NPGCS precast shear wall specimens indicated that the mechanical properties of NPGCS is good enough to match the “equal to cast-in-situ” mechanical design requirements. But in high-rise residential precast shear wall buildings, precast shear walls bear higher seismic load and work together with connecting beams formed by windows opening. So, the seismic performance of NPGCS shear wall combined with connecting beams should also be taken into consideration.

In 2014, the NPGCS was applied in a 33 stories’ precast shear wall high-rise residential building in Haimen city in China. The building is $26.3\text{ m} \times 15.9\text{ m}$ in plain, and the structure height is 102.7 m. As the first high-rise precast residential building in China, its seismic fortification intensity is the 7th degree with a 0.15 g earthquake ground motion acceleration, where g is the gravity acceleration. To achieve better seismic security, the bottom five floors use cast-in-situ construction approach while the above 28 floors applied the NPGCS precast shear wall technology. Early seismic time-history evaluation [7] for whole precast structure was carried out to evaluate seismic reliability. In the seismic time-history evaluation, the labeled precast shear walls in the sixth floor shown in Figure 3 were the most

important components whose concrete material damage was serious, which is shown in Figure 4. The sixth floor was the key floor in this building as the bottom five floors are cast-in-situ and floors started from the sixth floor applied the NPGCS precast shear wall technology, so the labeled precast walls in Figure 3 were selected out from the sixth floor and tested by experiment as a spatial model. Considering the major influence of bending moment for high-rise shear wall structure, two floor heights were selected as the spatial model height to enlarge bending moment influence. Early low-cyclic reversed lateral loads test on NPGCS precast shear wall spatial structure model proved the reliability and evaluated the seismic properties. In this paper, the accurate finite-element numerical simulation method was studied and adopted to understanding mechanical details on the NPGCS spatial model for further step.

2. Finite-Element Model Details

2.1. Model Sizes. Limited by experimental conditions, the NPGCS spatial model was 1/2 of the real structure size. The sizes of the finite-element model were same to the experimental model sizes. The sizes and reinforcements in each component are shown in Table 1. The assemble details are shown in Figure 5. The sizes of the NPGCS spatial are shown in Figure 6. The concrete strength grade was C35. The strength grade of main steel bars was HRB400 (C).

2.2. Loading Simulation. The experimental test setup is shown in Figures 7 and 8. The specimen’s total size in plain is $4.8\text{ m} \times 2.1\text{ m}$ with the height of 3.6 m. Limited by computer simulation conditions, only single-direction push over load was applied on the spatial model top coupling point RP-1, and the red vector is shown in Figure 9. According to early finite-element study results of the 33 stories precast building structure, the design axial load ratio was 0.24 and the axial compression load was 2400 kN. In the simulation, a body force of 15.6 N/mm^2 , the yellow vectors in Figure 9, will be applied in the loading beam part to simulate the 2400 kN axial load, shown in Figure 9.

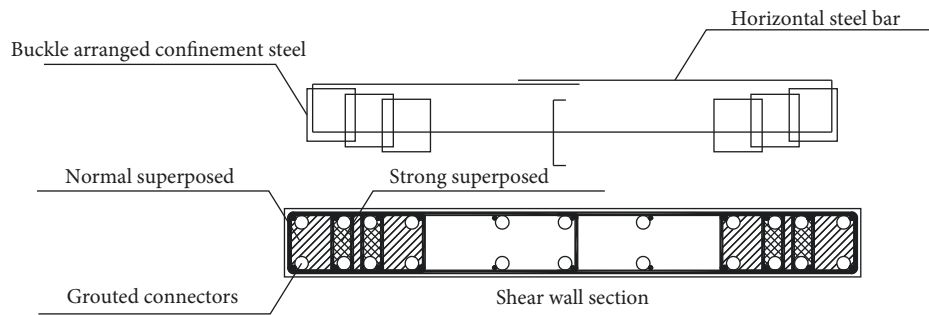


FIGURE 2: Buckle arranged confinement steel hoops and the superposed area.

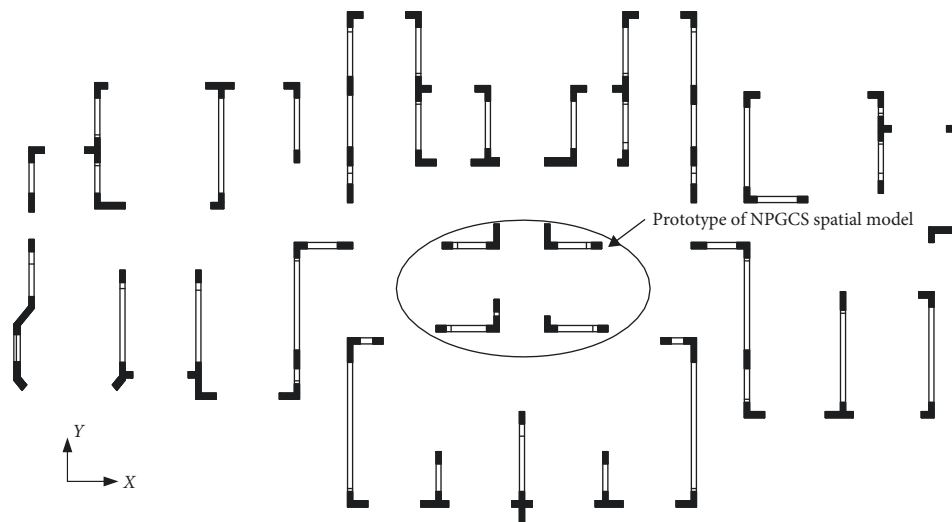


FIGURE 3: The NPGCS spatial model prototype in the key floor.

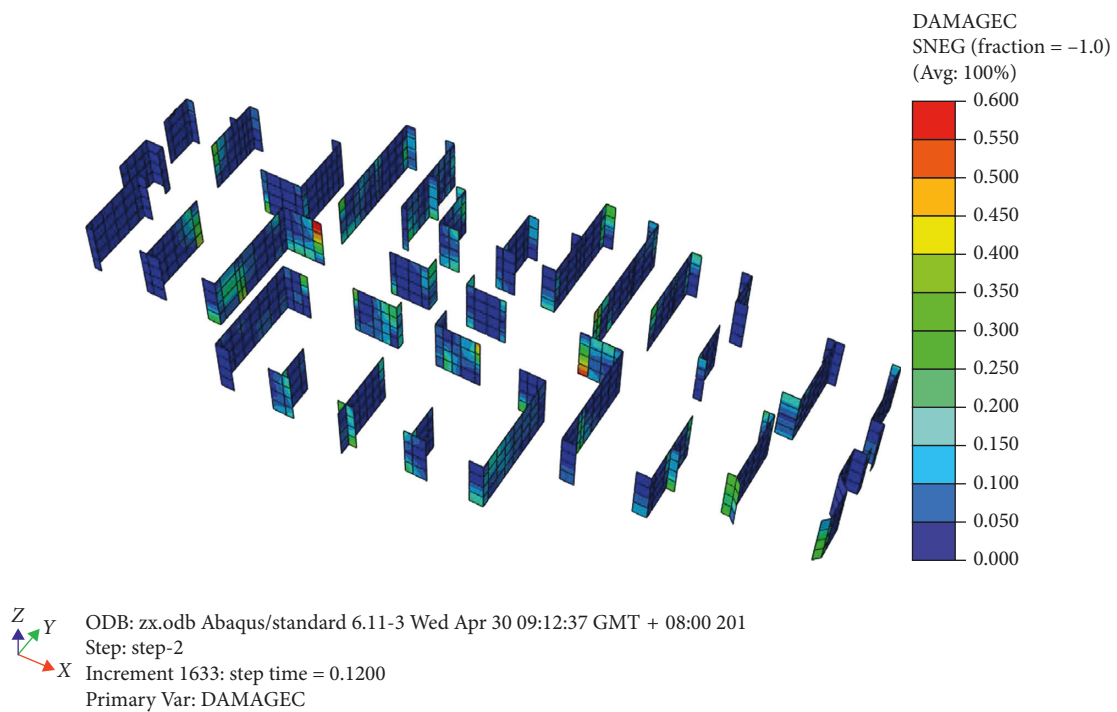


FIGURE 4: Concrete compressive damage of vertical shear walls in the key floor.

TABLE 1: Sizes and reinforcements in NPGCS spatial model components (mm).

Component number	Component name	Component sizes (height \times width \times thickness)	Vertical steels	Horizontal steels/confinement steels
QZ-1	Flange of T-section shear wall	1190 \times 400 \times 100	12C6 mm	A6@100 mm
QZ-2	Web of T-section shear wall	1340 \times 850 \times 100	8C6 + 10A6 mm	A6@100 mm
DZ-1/2	Experimental loading base	2390 \times 900 \times 350	36C4 mm	C8@50 mm
LL-1	Longitudinal superposed connecting beam	150 \times 100 \times 920	3C8 mm	C6@50 mm
LL-2	Inside transverse superposed connecting beam	100 \times 100 \times 970	3C12 mm	C6@50 mm
LL-3	Outside transverse superposed connecting beam	100 \times 200 \times 1270	3C12 mm	C6@50 mm
DB-1/2	Superposed slab	50 \times 945 \times 1270	A6@100 mm	A6@100 mm

2.3. Material Stress-Strain Models. Concrete applied the concrete damage stress-strain model. The material strengths are determined by the “Code for design of concrete structures” (GB50010-2010) [10]. The stiffness for concrete was determined by the ACI which related with dry dentist of aggressive and axial compress strength of concrete (MPa). The steel bar stress-strain model applied the double-line model, in which the stress will firstly be elastic with strain and keep being the yielding strength after steel bar yielded.

2.4. Precast Joint Interface Simulation. Precast joint interface actions include concrete friction, concrete compression, actions between steel bars and concrete, and the dowel shear action on connecting steel bars. All the four actions were disposed by the following methods.

2.4.1. Concrete Friction. The face-to-face contact element was applied to simulate concrete joint interface friction and compression, which includes horizontal action and vertical action. The horizontal action is related with concrete friction. In the face-to-face contact element, no slip occurred when joint interface shear stress is smaller than the static friction strength, while slip is also allowed when shear stress on contacted surfaces is larger than the static friction strength and the surface friction stress is equal to the static friction strength. The static friction ratio is 0.4 [7].

2.4.2. Concrete Compression. The vertical action in face-to-face contact element related with concrete compression action and the “hard” contact will be applied, in which interface compressive stress exists when contacted element surface’s gap opening is zero and contacted element surface’s gap opening will take place when the compressive force is zero.

2.4.3. Steel Bars and Concrete Actions. Early experimental tests show that no steel bar connecting failure occurred, and the single NPGCS connector can completely match the connecting strength requirements. So, the adhesive action between concrete and steel bars in all precast joint interfaces

was ignored to achieve safety strength and available calculation. All steel bars were embedded in the whole model.

2.4.4. Dowel Shear Action. Dowel shear action will cause steel bar bending and shear shown in Figure 10 and will reduce the yield strength according to the Von Mises strength rule [4]. The experiment collected results also proved the existence of joint interface slips shown in Figure 11, which has also been proved to be related with crack distribution. In order to achieve the balance between simulation accuracy and speed, all the connecting steel bars will use the beam element, which is able to simulate the shear and bending of steel bars, while other steel bars will adopt the truss element which only simulates the tensile and compressive stress on steel bars.

Apart from the above actions, early experiment observed that shear wall cracks and damage gathered at the first floor while the second-floor shear walls remain intact, so only the first-floor shear wall joint interfaces were considered. With the above disposals and assumptions, the spatial model contains 16 precast joint interfaces surface couples shown in Figure 12, including three types of shear wall-base joint interface, shear wall-beam joint interface, and beam-floor joint interface.

2.5. Element Types. Concrete parts used the C3D8R solid space element containing 8 nodes and 6 faces. The connecting steel bars applied the B31 linear beam element while other steel bars applied the T3D2 truss element. The concrete parts of the whole spatial model are shown in Figure 13, and the steel bars are shown in Figure 14.

3. Simulation Results

3.1. Strength and Stiffness. Strengths of finite-element simulation and experiment test are shown in Table 2. The ultimate strength of finite-element simulation is 927.08 kN, which is close to the experimental ultimate capacity of 1042 kN and 946.1 kN for forward loading and opposite loading, respectively. The relative error between finite-element simulation strength to the average experimental ultimate strength (994.05 kN) is only -0.67% .

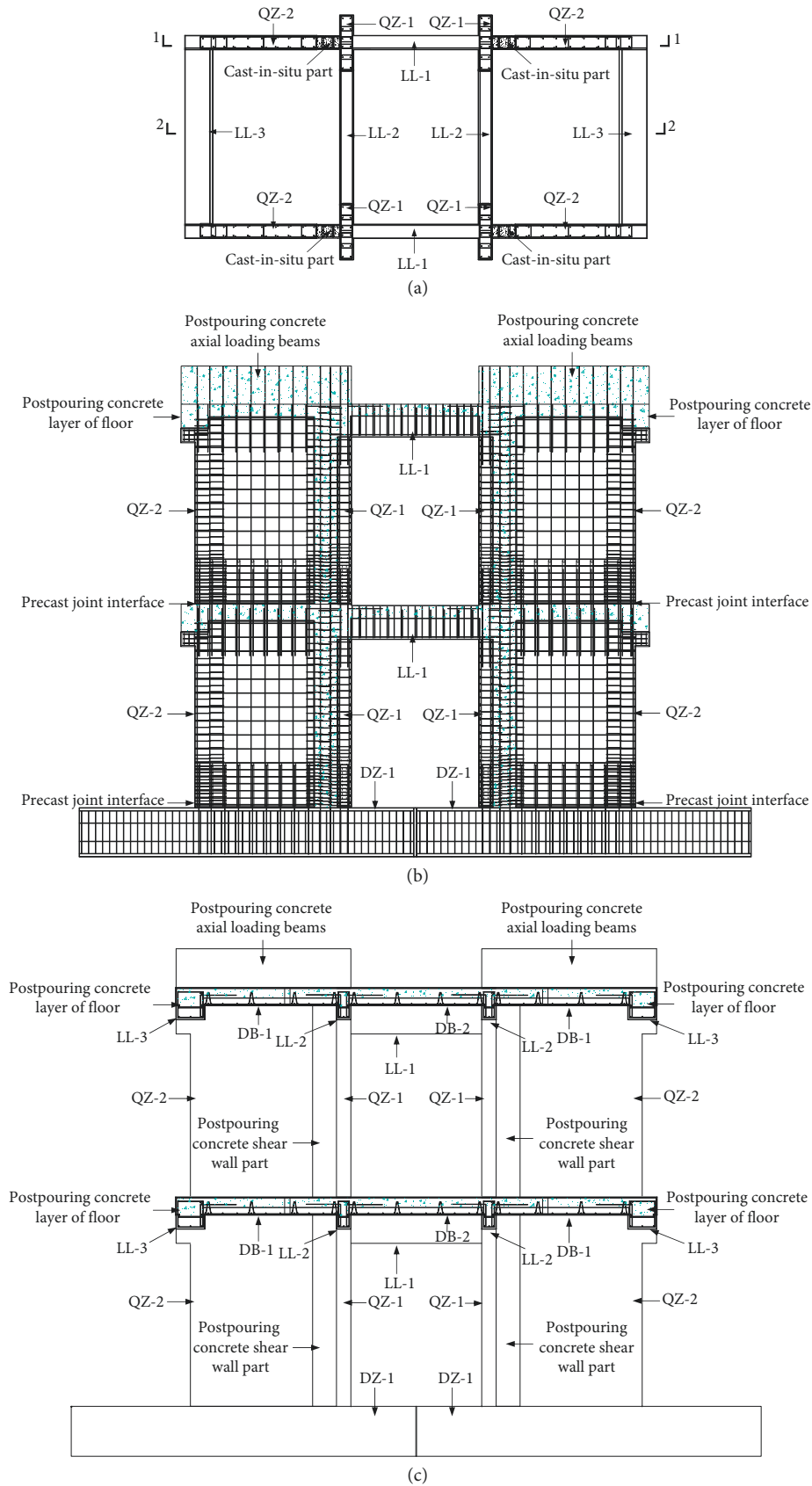


FIGURE 5: The assemble details of the NPGCS spatial model. (a) Components of the NPGCS spatial model in plan, (b) 1-1 sectional view of the NPGCS spatial model, and (c) 2-2 sectional view of the NPGCS spatial model.

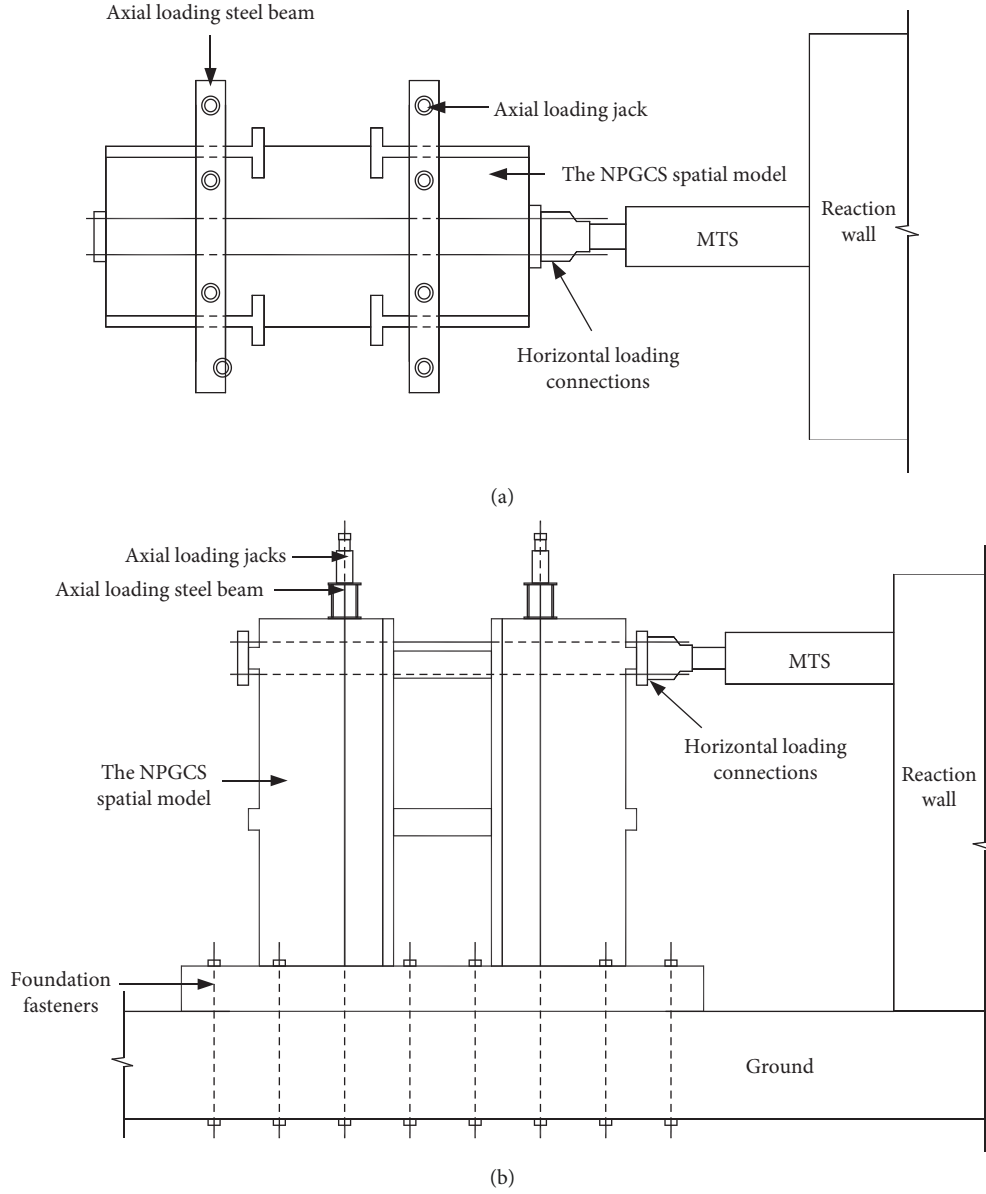


FIGURE 7: Experimental test setup. (a) Plan view. (b) Elevation view.

coefficient of seismic strength, shown in the following equations:

$$N \leq \frac{1}{\gamma_{RE}} \{ \alpha_1 f_c [\xi b h_0 + (b'_f - b) h'_f] + f'_y A'_s - \sigma_s A_s + N_{sw} \},$$

$$Ne = \frac{1}{\gamma_{RE}} \left\{ \alpha_1 f_c \left[\xi (1 - 0.5\xi) b h_0^2 + (b'_f - b) h'_f \left(h_0 - \frac{h'_f}{2} \right) \right] + f'_y A'_s (h_0 - a'_s) + M_{sw} \right\},$$

where

(1)

where γ_{RE} is the adjustment coefficient of seismic strength and will be 0.85 for shear wall and N is the axial load acting on shear wall section.

$$e = e_i + \frac{h}{2} - a,$$

$$e_i = \frac{M}{N} + e_a,$$

$$N_{sw} = \left(1 + \frac{\xi - \beta_1}{0.5\beta_1\omega} \right) f'_{yc} A_{sw}, \quad (2)$$

$$M_{sw} = \left[0.5 - \left(\frac{\xi - \beta_1}{\beta_1\omega} \right)^2 \right] f_{yw} A_{sw} h_{sw},$$



FIGURE 8: The test setup and specimen in reality.

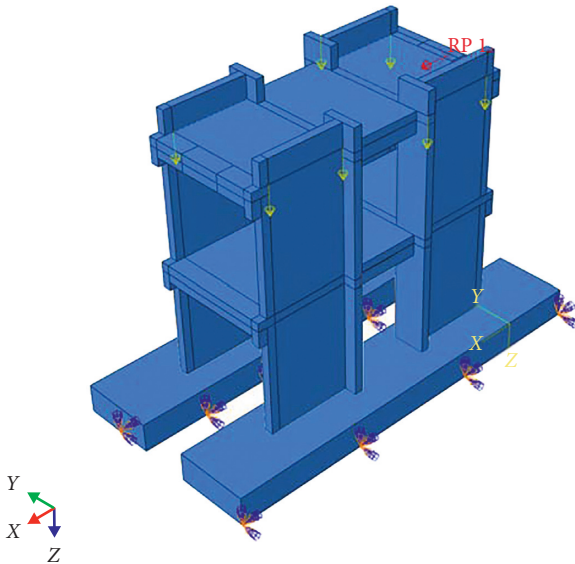


FIGURE 9: Loading simulation and boundary condition.

The experimental ultimate strength values exceed those of finite-element simulation and the equation-calculated strength according to equations (1) and (2), which are from the “Code for design of concrete structure” in China, indicating that the NPGCS connector successfully achieved good connecting properties in strength and matched the seismic requirements for high-rise buildings in the 7-degree seismic fortification intensity.

Significant differences exist between the finite-element simulated and the experimental load-displacement curves shown in Figures 15–17. The initial stiffness of finite-element simulation is higher than the experimental initial stiffness. The reasons include (1) the finite-element method used limited free degree quantity of nodes to simulate the infinite nodes free degree in reality and (2) the loading equipment end gap opening and slip enlarged the tested displacement and reduced the stiffness.

The displacement results are shown in Table 3, and the experimental displacements at ultimate capacity points are 33.34 mm and 27.34 mm for forward loading and opposite loading, respectively, which are lower than 52.8 mm of the finite-element simulated displacement at an ultimate capacity point. Additionally, the experimental curves declined rapidly after the ultimate capacity point while there was nearly no strength decline in the finite-element simulated curve. So, the experimental load-displacement curve shows more brittle properties than the finite-element simulated curve and the reasons include (1) by applying cyclic loads in the experiment, the concrete damaged and steel bar plastic deformed completely, while finite-element simulation for single-direction loading cannot ensure same concrete damage and steel bar plastic deformation and (2) steel bar fractured in reality, while the stress-strain model of steel bar in finite-element simulation only considered the elastic and yielding stages.

According to all the results above, it can be proved that the finite-element simulated strength can match the accuracy requirement, while the stiffness and displacement vary to the experimental results. So, this finite-element simulation method for precast shear wall can partially supply stress and material damage data in the ultimate strength situation.

3.2. Concrete Damage. For convenient description, the names of components and joint interfaces are shown in Figure 18.

3.2.1. Concrete Compressive Damage and Failure Mode. Figure 19 shows the concrete compressive damage distribution in the failure stage. The peak value of the concrete compressive damage factor exceeded 0.8 (1.0 means complete concrete damage and 0.0 means concrete intact) and compressive damage gathered at the sectional edge of Joint 1 in C and D shear walls, while the concrete compressed damages at other areas are relatively low. As the concrete compressive damage gathered at the limited sectional edge area close to Joint 1 in C and D shear walls while most of the other areas are almost undamaged, the concrete compressive damage of finite-element single-direction loading is uncompleted, which is also the main reason causing differences between finite-element analysis and experimental load-displacement curves in Figures 15–17. It should be noticed that the finite-element concrete compressive damage coordinates with the failure mode in which the web shear wall edge was compressively damaged in Figure 20.

Figure 20 shows the experimental failure mode of precast shear walls. The failure of precast shear walls were typical

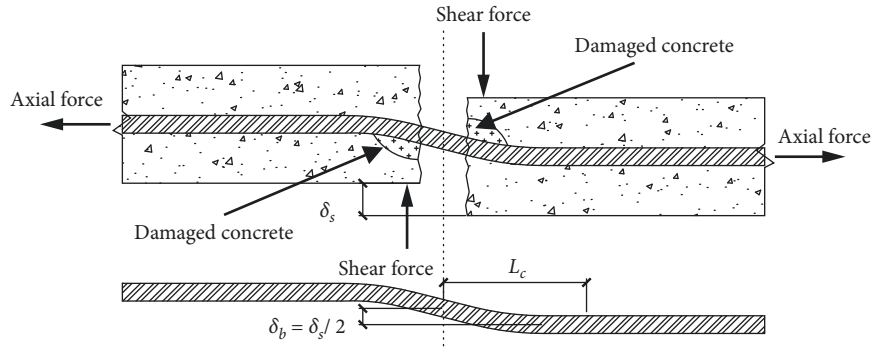


FIGURE 10: The steel bar dowel shear reaction at joint interface.

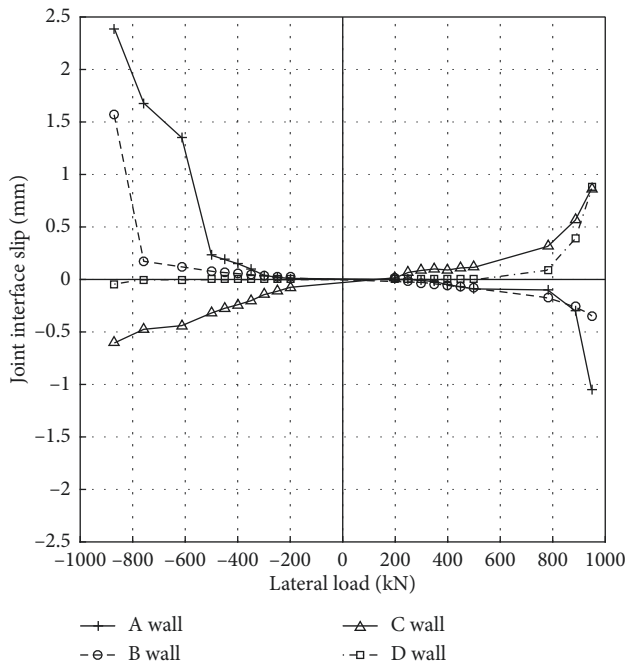


FIGURE 11: Lateral load-slip curves for precast shear walls.

bending-shear failures as the two floors of the shear wall enlarged the moment-shear ratio. In the web edge of the Joint 1 section, the concrete was badly compressive damaged, and some steel bars were pulled to be fractured. A part from the concentrated fracture of steel bar at Joint 1, no failure extending into the NPGCS was found in the experimental test, which successfully proved that the NPGCS completely match the fully force transferring requirements, and the ignorance of adhesive between concrete and steel bars is reasonable in the finite-element simulation.

3.2.2. Concrete Tensile Damage and Cracks. The concrete tensile damage ratio distribution is shown in Figure 21. The tensile damage area concentrated at the first-floor shear walls, while the concrete tensile damage at the second floor was very low, coordinating with the first-floor concentrated crack (Figure 22) and failure in the spatial model experiment (Figure 20). The concrete tensile damage in the A/B shear

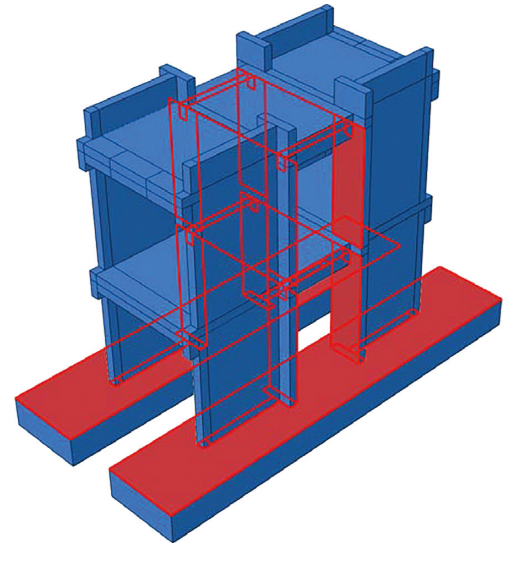


FIGURE 12: The concrete contact surfaces of NPGCS finite-element spatial model.

walls is more serious than that in the C/D shear walls, caused by the enlarged concrete flange area. It should be noticed that the tensile damage factor gradient line closely coordinated with the tensile shear-bending crack area in Figure 22, which is nearly horizontal at the shear wall edge while cline into an approximate 45-degree shear-bending crack at the middle part of shear walls.

Figure 22 shows the crack distributions on experimental shear walls and the crack distribution area in a unidirectional loading closely coordinate with the concrete tensile damage ratio distribution [13, 14]. The cracks were bending-shear cracks and concentrated at the first floor but not at the second floor, indicating that the first-floor shear walls are key components. On the contrast, other joints including Joint 2, Joint 4, and Joint 5 were intact during the test and can be neglected in finite-element simulation.

3.3. Stress Distributions

3.3.1. Concrete Stress. Figure 23 shows the concrete stress distribution in the ultimate strength stage. The shear wall

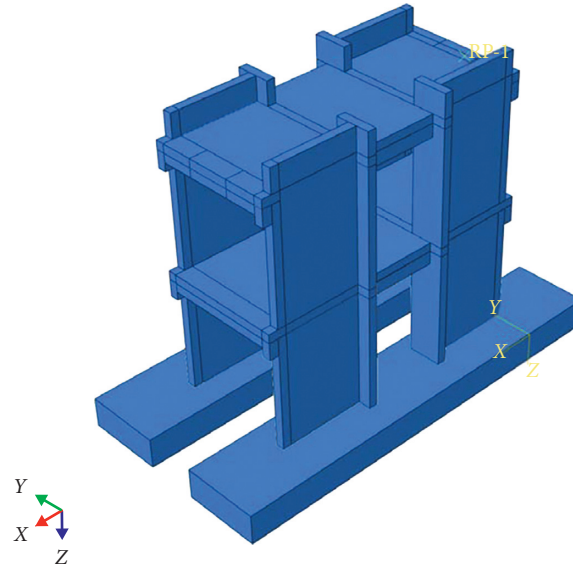


FIGURE 13: The NPGCS finite-element spatial model.

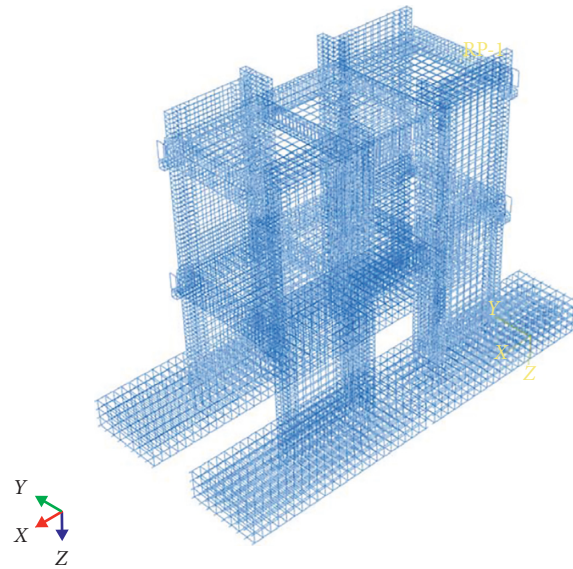


FIGURE 14: The steel bars of NPGCS finite-element spatial model.

TABLE 2: Strengths of the NPGCS spatial model.

	Experimental crack load (kN)	Experimental yield load (kN)	Experimental ultimate load (kN)
Forward	300	859.4	1042.5
Opposite	300	764.5	946.1

compressive edge bears large compressive stress [15, 16]. The large compressive stress declined as the moment-bending affection declined while shear affection increased with an increase in position height. According to stress distributions, the stress of the C/D shear wall has a higher peak value and more extensive distribution area than that of the A/B shear wall, caused by the flange part area enlargement leading to a compressive stress reduction.

3.3.2. Reinforcement Stress. The reinforcement stress distribution in the ultimate strength stage is shown in Figure 24. For the A/B shear wall, it is obvious that very large compressive and tensile stress exist on flange edge area reinforcement and web edge area reinforcement, respectively. The compressive stress on flange edge area reinforcement concentrated close to the Joint 1, while tensile stress on web edge area reinforcement concentrated on two areas of above

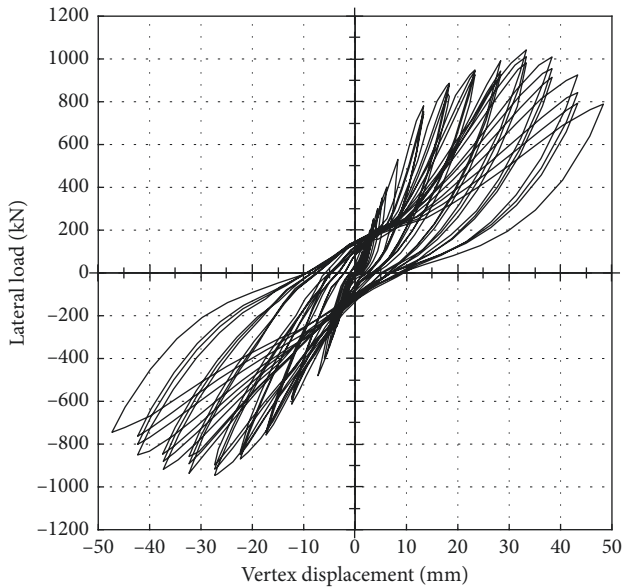


FIGURE 15: The force-displacement hysteretic curve.

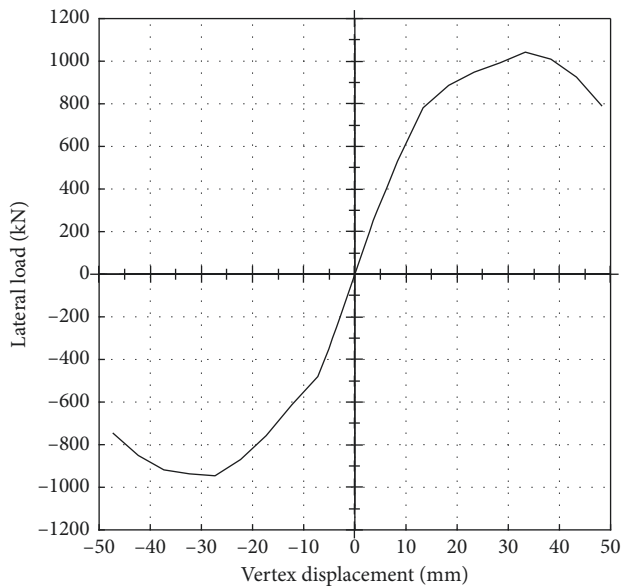


FIGURE 16: The force-displacement skeleton curve.

and very close to Joint 1, and the tensile stress distribution area at the area above to Joint 1 is larger than that close to Joint 1. This coordinated with the first observed crack that occurred at approximately 350 mm higher to Joint 1 in the experiment, which also proved the new two weak sections in precast shear walls generated by the overlapped connecting steel bars and shear wall vertical steel bars. For the C/D shear walls, the phenomenon same with that in A/B shear walls also exist, in which the compressive reinforcement stress concentrated at the area close to Joint 1 while the largest tensile stress and main distribution area concentrated at the two weak sections generated at the two overlapping ends of connecting steel bars.

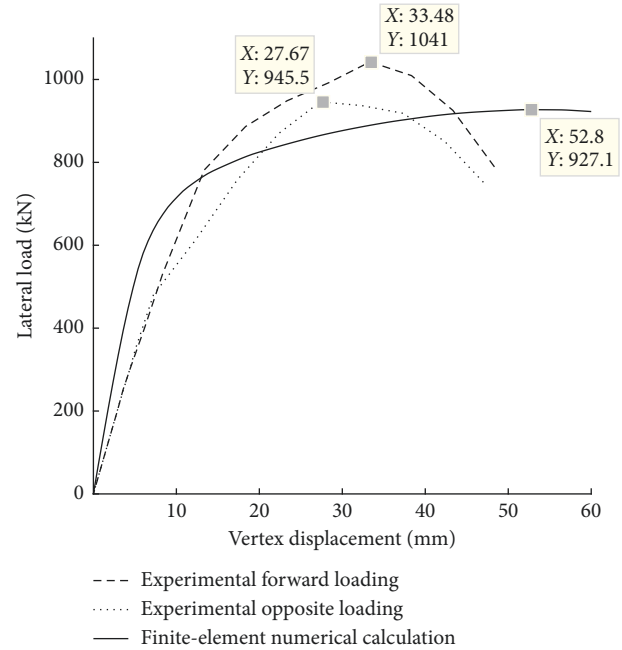


FIGURE 17: The lateral load-vertex displacement of the NPGCS finite-element spatial model.

4. Conclusions

By the finite-element simulation on the NPGCS spatial model and comparison between finite-element simulation results and experimental results, the following conclusions can be obtained:

- (1) The face-to-face contact element and beam element are applied to simulate precast concrete joint interface and steel bar dowel shear action. According to the finite-element simulation, the NPGCS spatial model can be partly accurately simulated by the finite-element simulation method. Especially for the ultimate strength, the relative error between finite-element simulation ultimate strength and the average experimental ultimate strength is only -0.67% .
- (2) The loading method in finite-element simulation influenced the simulation accuracy of stiffness and displacements. According to the concrete compressive damage distribution obtained from the finite-element simulation, single-direction loading only caused partial concrete compressive damage while cyclic loading can achieve a complete concrete damage. So, it is suggested that the cyclic loading simulation method should be taken into finite-element simulation.
- (3) The concrete damage ratio, including the compressive damage ratio and tensile ratio, also concentrated at the first floor and differed depending on shear wall loading directions. Apart from that, the compressive damage distribution reflects final failure mode and the tensile damage distribution coordinating with the experimental cracks distribution area in unidirectional loading.

TABLE 3: Displacements and ductility of the NPGCS spatial model.

	Yield displacement (mm)	Ultimate displacement (mm)	Failure displacement (mm)	Ductility factor
Forward	17.06	33.34	44.77	1.95
Opposite	17.64	27.34	44.53	1.55

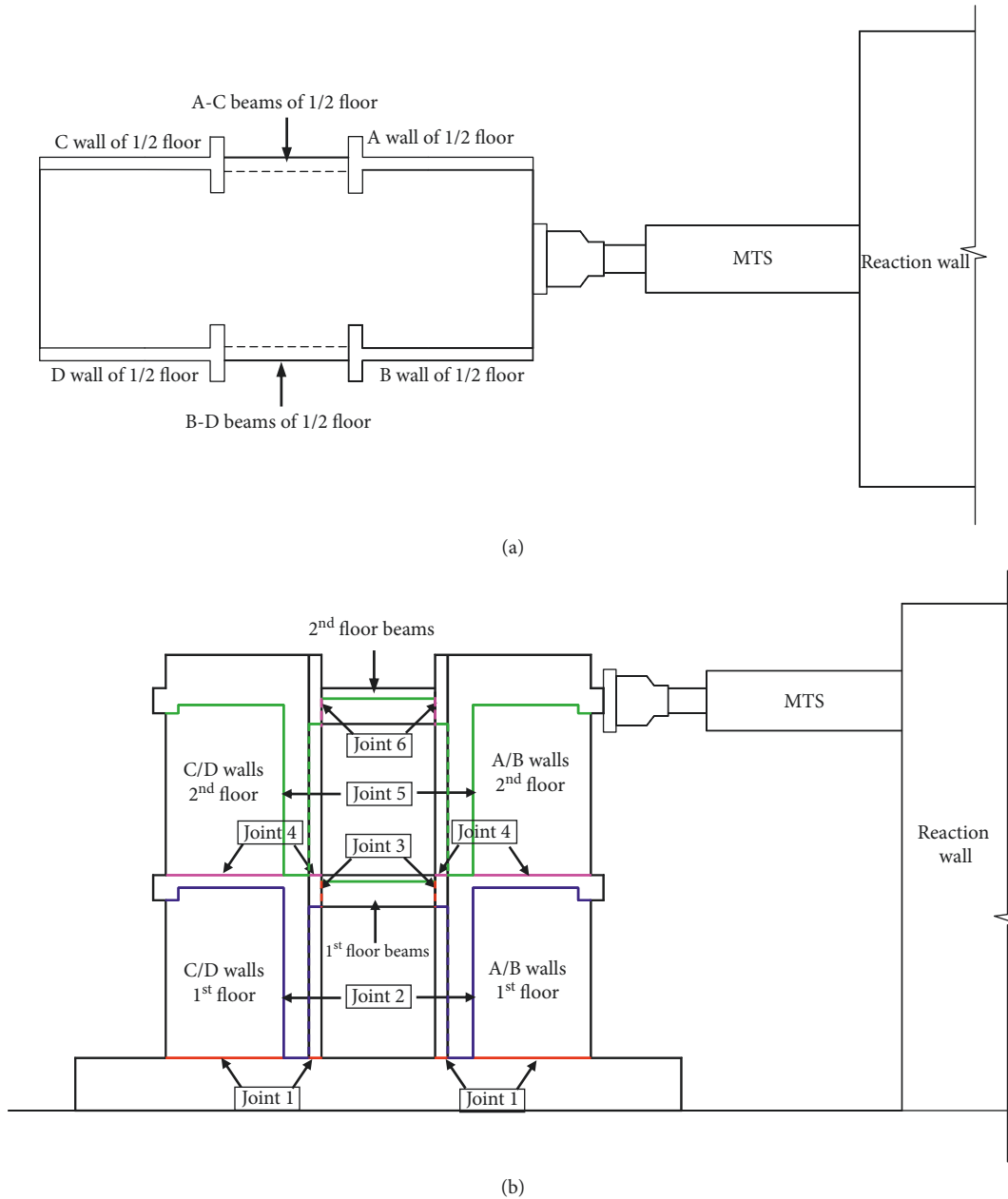


FIGURE 18: Components and joint interfaces names. (a) Plan view. (b) Elevation view. Note: Joint 1 (red) contains eight joints belonging to the flange and web area joints of A/B/C/D walls at the 1st floor. Joint 2 (blue) contains the initial and postconcrete pouring joints of shear walls at the 1st floor. Joint 3 (red) contains the beams-postconcrete pouring shear wall joints at the 1st floor. Joint 4 (purple) contains eight parts belonging to the flange and web area joints of A/B/C/D walls at the 2nd floor. Joint 5 (green) contains the initial and postconcrete pouring joints of shear walls at the 2nd floor. Joint 6 is the beams-postconcrete pouring shear wall joints at the 2nd floor.

(4) Stress of concrete and reinforcement steel bars concentrated to distribute at the first floor while differed according with compressive or tensile

situation. Compressive stress concentrated close to the shear wall-base joint while tensile stress concentrated at two areas above and close to shear wall-

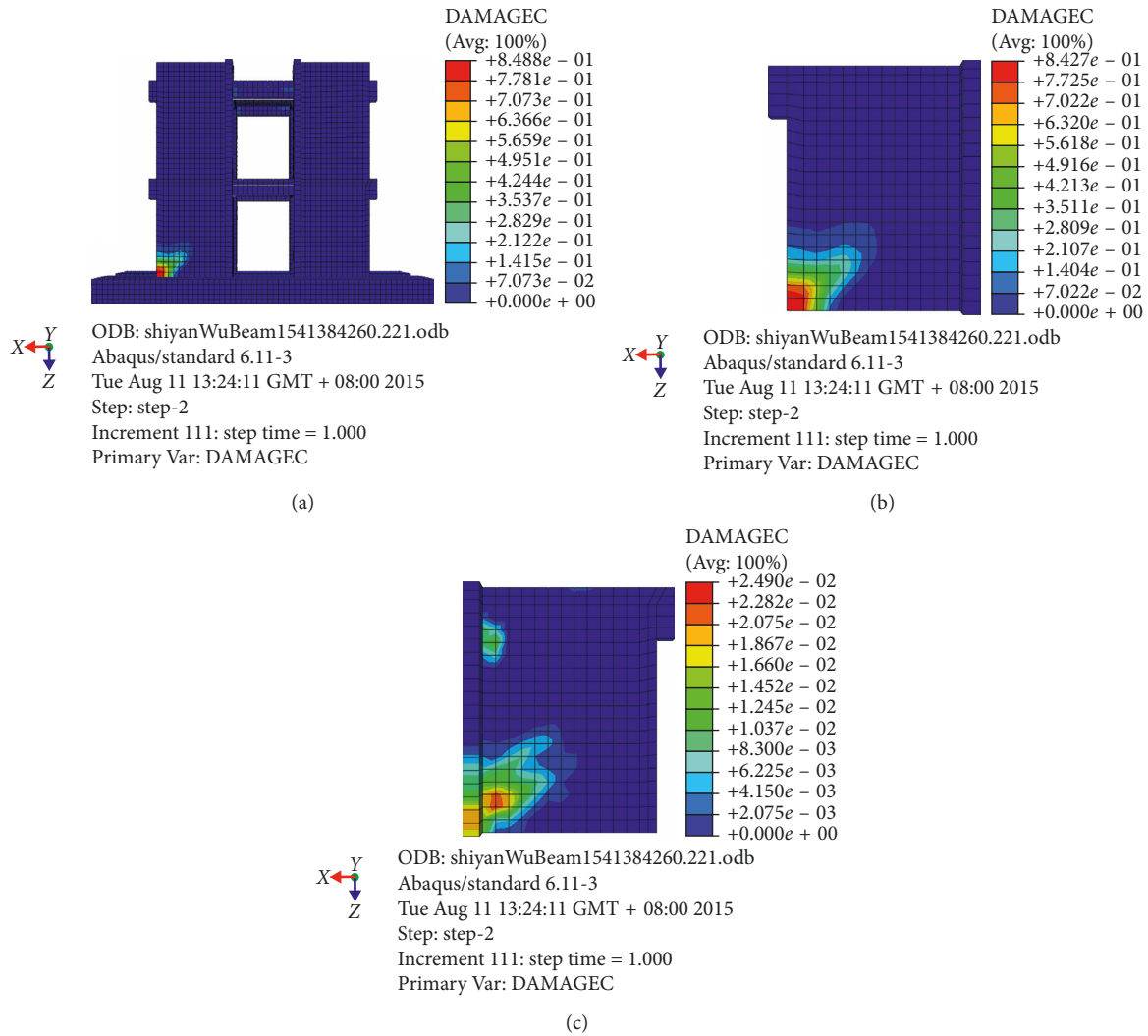


FIGURE 19: Concrete compressive damage ratio distribution of the NPGCS spatial model. (a) Concrete compressive damage ratio distribution of the whole NPGCS spatial model. (b) Concrete compressive damage ratio distribution on 1st floor web compressive panel of the whole NPGCS spatial model. (c) Concrete compressive damage ratio distribution on 1st floor flange compressive panel of the whole NPGCS spatial model.



FIGURE 20: Continued.



FIGURE 20: Damage of precast shear walls at the base position. (a) Precast shear wall A. (b) Precast shear wall B. (c) Precast shear wall C. (d) Precast shear wall D.

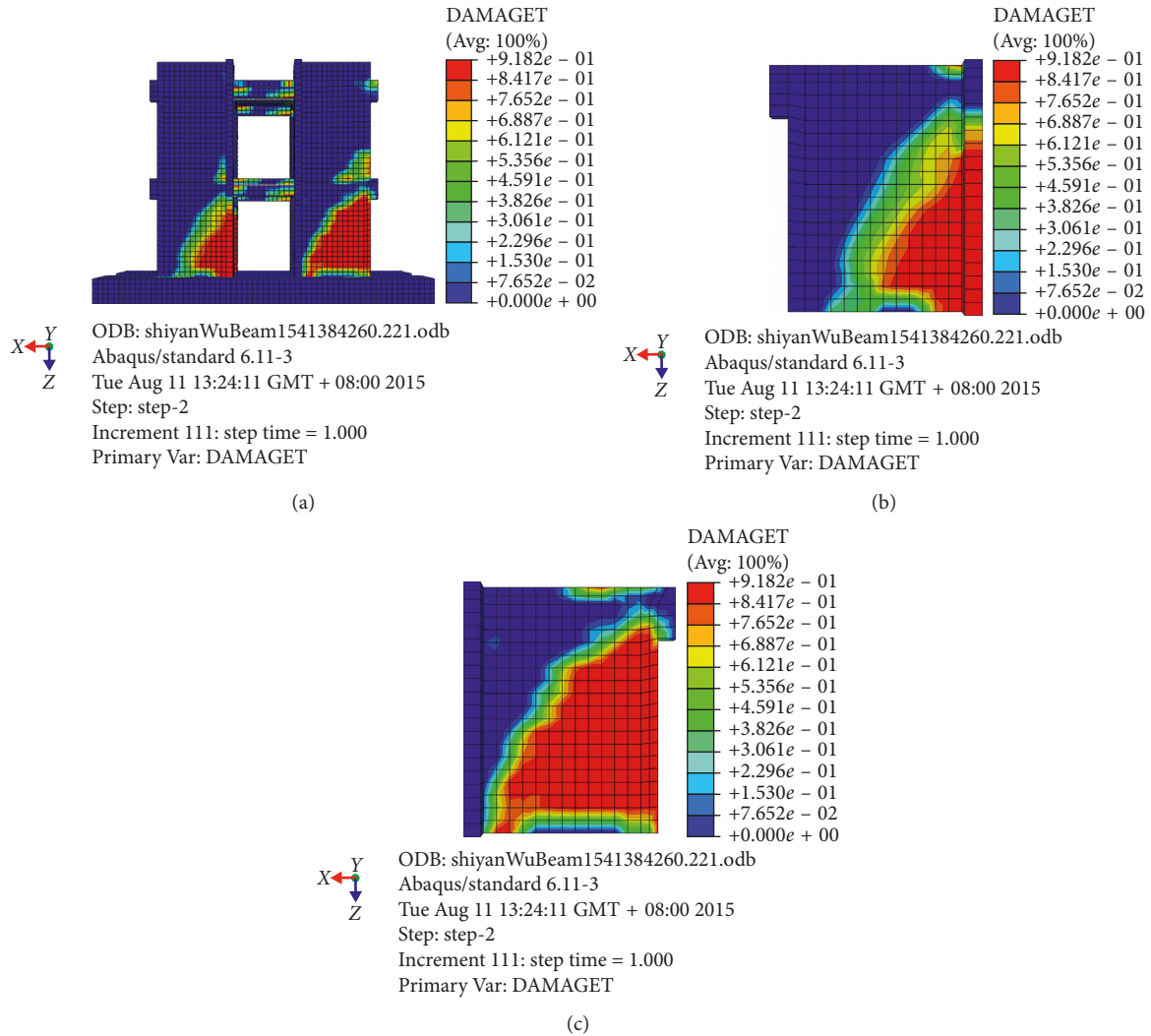


FIGURE 21: Concrete tensile damage ratio distribution of the NPGCS spatial model. (a) Concrete tensile damage ratio distribution of the whole NPGCS spatial model. (b) Concrete tensile damage ratio distribution on the 1st floor web compressive panel of the whole NPGCS spatial model. (c) Concrete tensile damage ratio distribution on the 1st floor flange compressive panel of the whole NPGCS spatial model.

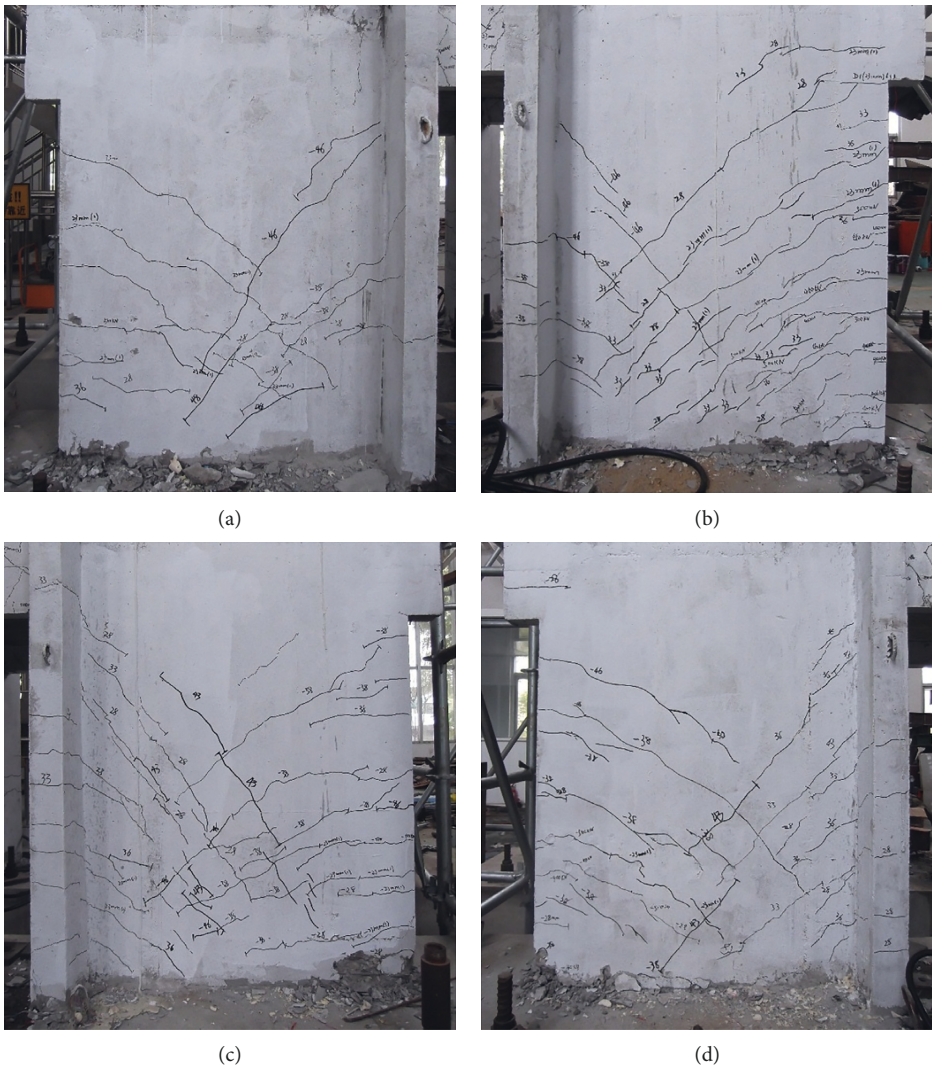


FIGURE 22: Cracks distribution on precast shear walls. (a) Precast shear wall A. (b) Precast shear wall B. (c) Precast shear wall C. (d) Precast shear wall D.

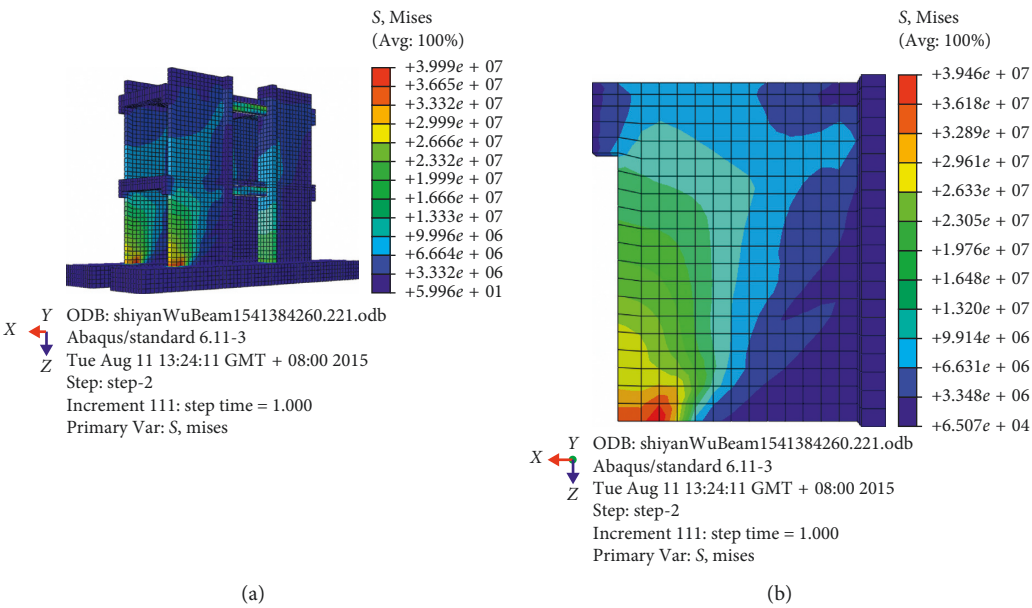


FIGURE 23: Continued.

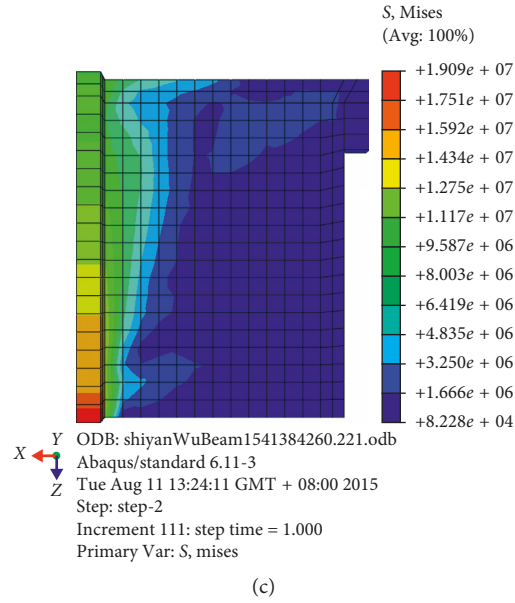


FIGURE 23: Concrete stress distribution on the NPGCS finite-element spatial model. (a) Concrete stress distribution of the NPGCS finite-element spatial model. (b) Concrete stress distribution on 1st floor web compressed panel of the NPGCS finite-element spatial model. (c) Concrete stress distribution on 1st floor flange compressed panel of the NPGCS finite-element spatial model.

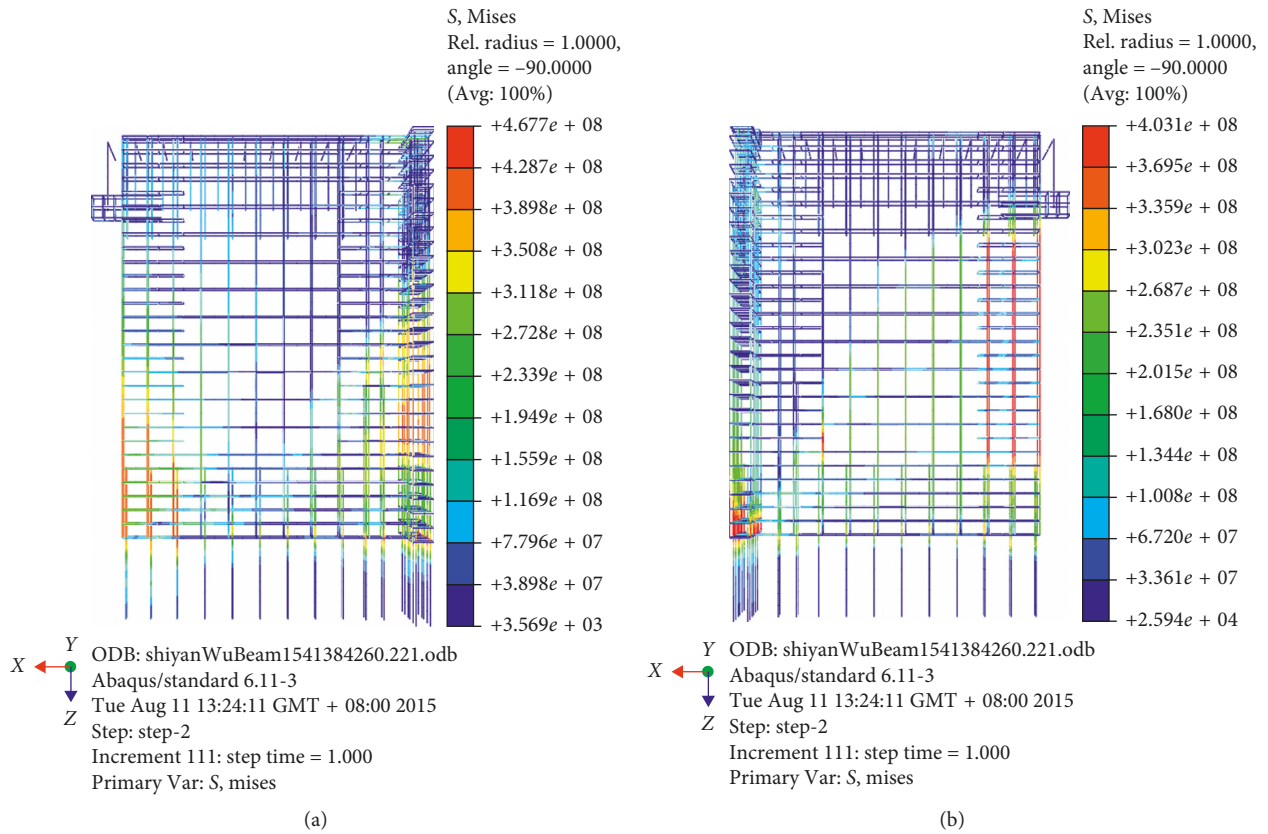


FIGURE 24: Steel bar stress distribution on the NPGCS finite-element spatial model. (a) Steel stress distribution on 1st floor web compressed panel of the NPGCS finite-element spatial model. (b) Steel stress distribution on 1st floor flange compressed panel of the NPGCS finite-element spatial model.

base joint, which proved the existence of two new weak sections in grouting connecting precast shear walls generated by the overlapping of connecting steel bars and shear wall vertical steel bars, observed in the experiment.

Data Availability

The data used to support the findings of this study are available from the corresponding author upon request.

Conflicts of Interest

The authors declare that they have no conflicts of interest.

Acknowledgments

Financial support from the National Natural Science Foundation for Young Scientists of China (Grant No. 51708260), the University Natural Science Foundation funded by the Jiangsu Province Government (Grant No. 2016TM045J), and the Natural Science Fund of Jiangsu (BK20141090).

References

- [1] J. Chen and Y. Su, "Prefabricated concrete shear wall structure and its connecting technology," *World Earthquake Engineering*, vol. 29, no. 1, pp. 38–48, 2013.
- [2] A. Belleri, "Displacement based design for precast concrete frames with not-emulative connections," *Engineering Structures*, vol. 141, pp. 228–240, 2017.
- [3] E. Musselman, M. Fournier, P. Mcalpine, and S. Sritharan, "Behavior of unbonded post-tensioning monostrand anchorage systems under short duration, high amplitude cyclical loading," *Engineering Structures*, vol. 104, pp. 116–125, 2015.
- [4] W. Zhang, J. Qian, J. Yu, H. Qin, and G. Liu, "Tests on seismic behavior of precast shear walls with cast-in-situ boundary elements and vertical distributed reinforcements spliced by a single row of steel bars," *China Civil Engineering Journal*, vol. 45, no. 10, pp. 89–97, 2012.
- [5] J. Qian, X. Yang, H. Qin, Y. Peng, J. Zhang, and J. Li, "Tests on seismic behavior of pre-cast shear walls with various methods of vertical reinforcement splicing," *Journal of Building*, vol. 32, no. 6, pp. 51–59, 2011.
- [6] Y. Zheng and Z. Guo, "Experimental study and finite element analysis on behavior of deformed gout-filled pipe splice," *Journal of Building*, vol. 37, no. 3, pp. 94–102, 2016.
- [7] D. Wu, S. Liang, Z. Guo, and X. Zhu, "The dynamic elastic-plastic time history analysis of precast high-rise shear wall structure," *Construction Technology*, vol. 22, pp. 15–19, 2014.
- [8] D. Wu, S. Liang, Z. Guo, and Q. Xiao, "Bending bearing capacity calculation of the improved steel grouted connecting precast wall," *Journal of Harbin Institute of Technology*, vol. 47, no. 12, pp. 112–116, 2015.
- [9] D. Wu, S. Liang, Z. Guo, X. Zhu, and Q. Fu, "The development and experimental test of a new pore-forming grouted precast shear wall connector," *KSCE Journal of Civil Engineering*, vol. 20, no. 4, pp. 1462–1472, 2015.
- [10] GB50010-2010, *Code for Design of Concrete Structures*, China Architecture & Building Press, Beijing, China, 2010.
- [11] JGJ 355-2015, *Technical Specification for Grout Sleeve Splicing of Rebars*, China Architecture & Building Press, Beijing, China, 2015.
- [12] GB/T 51231-2016, *Technical Standard for Assembled Buildings with Concrete Structure*, China Architecture & Building Press, Beijing, China, 2016.
- [13] H. Yang, M. Omidalizarandi, X. Xu, and I. Neumann, "Terrestrial laser scanning technology for deformation monitoring and surface modeling of arch structures," *Composite Structures*, vol. 169, pp. 173–179, 2017.
- [14] H. Yang, X. Xu, W. Xu, and I. Neumann, "Terrestrial laser scanning-based deformation analysis for arch and beam structures," *IEEE Sensors Journal*, vol. 17, pp. 4605–4611, 2017.
- [15] H. Yang, X. Xu, and I. Neumann, "Deformation behavior analysis of composite structures under monotonic loads based on terrestrial laser scanning technology," *Composite Structures*, vol. 183, pp. 594–599, 2017.
- [16] H. Yang, X. Xu, and I. Neumann, "Laser scanning-based updating of a finite-element model for structural health monitoring," *IEEE Sensors Journal*, vol. 16, pp. 2100–2104, 2016.

